JOURNAL OF COMPUTATIONAL PHYSICS 1, 87-118 (1966)

An Eulerian Differencing Method for Unsteady Compressible Flow Problems

RICHARD A. GENTRY, ROBERT E. MARTIN, AND BART J. DALY

University of California, Los Alamos Scientific Laboratory,
Los Alamos, New Mexico

ABSTRACT

An Eulerian finite difference method is presented which can be used with a high-speed computer to solve the time-dependent equations of motion for the compressible flow of a fluid. The difference equations are described in detail, and the nature of the truncation errors introduced by the numerical approximations is discussed, as are the stability properties of the equations. Three solutions involving time-dependent flow in two space dimensions are described and analyzed: the diffraction of a weak shock travelling through a *z*-shaped tunnel, the interaction of a supersonic blunt body with a plane shock wave, and the passage of a plane shock over a conical body. Good agreement with experimental data is obtained in all cases where comparisons are made.

INTRODUCTION

The development of high-speed computers has made it possible to solve a wide variety of complex time-dependent flow problems by using numerical techniques to solve the equations of motion for compressible fluid dynamics. Various methods are available for solving certain classes of problems, but each of the known methods has certain limitations. Lagrangian differencing techniques give good results with fine resolution for problems where the fluid distortions are relatively small. However, they are not suitable for cases involving large fluid distortions since the computing mesh becomes very irregular, leading to large errors as well as severe computational instabilities. The Particle-in-Cell (PIC) method, a combined Eulerian-Lagrangian scheme, has been applied successfully to solve a wide variety of multifluid problems where the fluid distortions are large [1, 2]. It utilizes Lagrangian fluid particles to transport mass, momentum, and energy through an Eulerian mesh of cells. While the use of these particles facilitates the calculation of multifluid problems, it also results in nonphysical fluctuations of the fluid quantities. Furthermore, the dual mesh system of the PIC method makes great demands on computer memory capacity and calculation time.

The technique described in this paper, known as the Fluid-in-Cell (FLIC) method, is an outgrowth of the work of Rich [3]. The difference equations are very similar to those used in the PIC method. However, it employs a different transport calculation which does not require the use of particles. This reduces the memory storage requirements for a given problem and reduces the computing time, since it is not necessary to compute the motion of the particles. Furthermore, the elimination of particles allows solutions which are free of the fluctuations which are characteristic of PIC. A version of the FLIC method is described here which is suitable for one material problems with symmetry about an axis or a plane, in which the solution is a function of two space variables and time. A general discussion of the important characteristics of the difference equations is presented and the results of several applications are discussed.

I. The Computing Mesh

In order to obtain a solution, the volume containing the fluid is first subdivided into a number of cells. A typical computational mesh is shown in Fig. 1. The center of a typical cell, denoted by the indices ij, is located at $(i + \frac{1}{2})\, \delta z$, $(j + \frac{1}{2})\, \delta r$. For problems in which a Cartesian coordinate system is used, each cell is a right parallelpiped with dimensions δr, δz, 1. If cylindrical coordinates are specified, then cell ij is a rectangular torus with inner and outer radii $j\delta r$, and $(j + 1)\delta r$, respectively, and width δz. The cells have the properties shown in Table I. Here S_j^z is the area of contact between cell ij and cell $i + 1, j$ open to z-direction flow, $S^r_{j+1/2}$ is the area of contact between cell ij and cell i, $j + 1$ open to r-direction flow, and V_j is the volume of cell ij.

The basic variables used to characterize the state of the fluid are the density, ρ, the z and r components of the fluid velocity, u and v, and the specific internal energy, I. Other thermodynamic quantities such as the

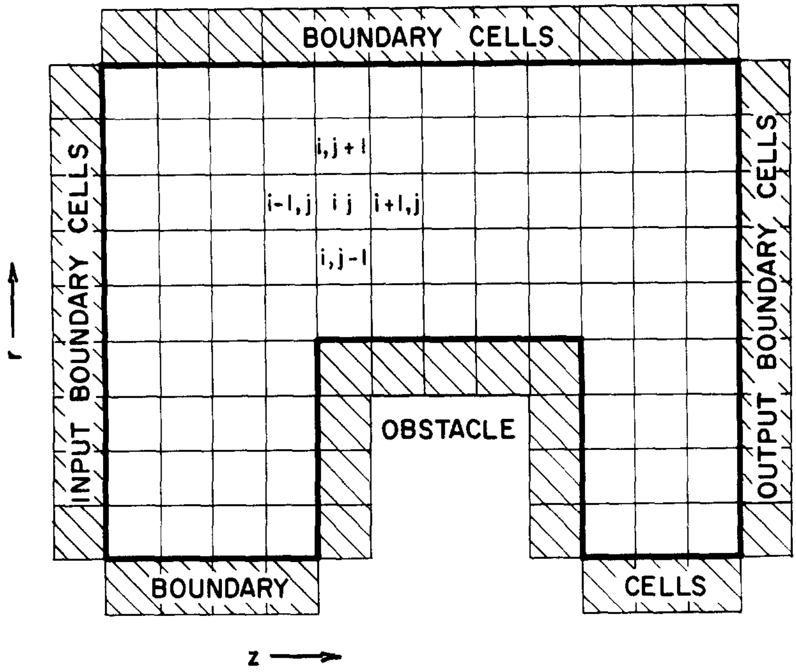

FIG. 1. The computing mesh.

pressure and sound speed are determined through the equation of state. For the examples presented, we have used an equation of state of the form

$$P = (\gamma - 1)\varrho I,$$

where γ, the ratio of the specific heats, can be a function of ϱ and I. The use of any other form, however, could be accomplished with equal ease.

TABLE 1

GEOMETRICAL PROPERTIES OF MESH CELLS

Property	Plane coordinates	Cylindrical coordinates
Volume (V_j)	$\delta r\, \delta z$	$2\pi(j + \frac{1}{2})\, \delta r^2\, \delta z$
Area (S_j^z)	δr	$2\pi(j + \frac{1}{2})\, \delta r^2$
Area $(S_{j+1/2}^r)$	δz	$2\pi(j + 1)\, \delta r\, \delta z$

II. The Difference Equations

Initial values of density, velocity, and specific internal energy are assigned to each mesh cell at the beginning of the problem. The value of each cell quantity is advanced in time using a finite difference approximation for the equations of motion of the fluid. The calculational scheme used here consists of two steps for each cycle: First, intermediate values are calculated for the velocities and specific internal energy, taking into account the effects of acceleration caused by pressure gradients. Second, transport effects are calculated.

The mass flow occurring across the cell boundaries during the time increment δt is determined using the intermediate values of velocity just calculated. The flow of momentum and energy are then computed by assuming that the mass which has crossed the cell boundaries carries momentum and energy corresponding to the intermediate values of velocity and specific energy of the donor cell. Then the final values for u, v, and I are computed by using the conservation of mass, momentum, and energy.

One can calculate either the specific internal energy or the specific total energy directly from the finite difference equations. The latter alternative is generally chosen for Eulerian techniques which retain the transport terms in the difference equations, because it lends itself more readily to energy conservation requirements. The FLIC method, however, calculates internal energy directly, using a difference form of the energy equation

$$\frac{DI}{Dt} = -P\nabla\cdot\mathbf{u}. \tag{1}$$

Here

$$\frac{D}{Dt} = \frac{\partial}{\partial t} + \mathbf{u}\cdot\nabla. \tag{2}$$

Energy conservation then follows by separating the calculation of acceleration effects from the calculation of transport effects and by the proper choice of time centering in Eq. (1) [4].

The quality of numerical results obtained is particularly sensitive to the method of representing the work term, $-P\nabla\cdot\mathbf{u}$. The form of the energy equation given below is practically identical with that used by Harlow in the PIC method [2]. This method, known as "zip-type" differencing, tends to eliminate spurious local oscillations in the solutions which occur when other schemes are used. Zip-type differencing is also effective in reducing the occurrence of negative values of the specific internal energy during the course of the calculation. In fact, the occurrence of negative values of I can be prevented by suitably restricting the value of δt if the fluid obeys a polytropic equation of state.

Assume that at time $t = n\delta t$ the following values are specified for each cell ij:

density: ϱ^n_{ij}
z-velocity component: u^n_{ij}
r-velocity component: v^n_{ij}
specific internal energy: I^n_{ij}

Values are then calculated for time $t = (n+1)\delta t$ as follows:

Step 1. The pressure P^n_{ij} is first calculated for each cell, using ϱ^n_{ij}, I^n_{ij} and the equation of state. Intermediate values for u, v, and I, denoted by a tilde, are now calculated using the relations

$$\tilde{u}^n_{ij} = u^n_{ij} - \frac{\delta t}{\varrho^n_{ij}\delta z}\left[(P+q)^n_{i+1/2,j} - (P+q)^n_{i-1/2,j}\right] \tag{3}$$

$$\begin{aligned}\tilde{v}^n_{ij} = v^n_{ij} - \frac{\delta t}{\varrho^n_{ij}}\Bigg\{&\frac{1}{2V_j}\left[S^r_{j+1/2}\left(P^n_{i,j+1} - P^n_{ij}\right) - S^r_{j-1/2}\left(P^n_{i,j-1} - P^n_{ij}\right)\right]\\ &+ \frac{1}{\delta r}\left(q^n_{i,j+1/2} - q^n_{i,j-1/2}\right)\Bigg\}\end{aligned} \tag{4}$$

$$\begin{aligned}\tilde{I}^n_{ij} = I^n_{ij} - \frac{\delta t}{\varrho^n_{ij}V_j}\Big\{&P^n_{ij}\left(S^r_{j+1/2}\,\bar{v}^n_{i,j+1/2} - S^r_{j-1/2}\,\bar{v}^n_{i,j-1/2}\right)\\ &+ \tfrac{1}{2}\,q^n_{i,j+1/2}\left(S^r_{j+1}\,\bar{v}^n_{i,j+1} + S^r_j\bar{v}^n_{ij}\right)\\ &- \tfrac{1}{2}\,q^n_{i,j-1/2}\left(S^r_j\bar{v}^n_{ij} + S^r_{j-1}\,\bar{v}^n_{i,j-1}\right)\\ &- \bar{v}^n_{ij}\,S^r_j\left(q^n_{i,j+1/2} - q^n_{i,j-1/2}\right) - \bar{u}^n_{ij}\,S^z_j\left(q^n_{i+1/2,j} - q^n_{i-1/2,j}\right)\\ &+ S^z_j\left[\bar{u}^n_{i+1/2,j}\left(P^n_{ij} + q^n_{i+1/2,j}\right) - \bar{u}^n_{i-1/2,j}\left(P^n_{ij} + q^n_{i-1/2,j}\right)\right]\Big\}.\end{aligned} \tag{5}$$

Here we use the notation:

$$\begin{aligned}P_{i+1/2,j} &= \tfrac{1}{2}\left(P_{ij} + P_{i+1,j}\right),\\ \bar{u}_{ij} &= \tfrac{1}{2}\left(u_{ij} + \tilde{u}_{ij}\right), \text{ etc.}\end{aligned} \tag{6}$$

The quantity $q^n_{i+1/2,j}$ is an artificial viscosity term which is added to enhance the stability properties of the difference equations in regions where the fluid velocity is small compared to the local sound speed, c^n_{ij}. The viscosity term is of the form

$$
\begin{aligned}
q^n_{i+1/2,j} &= Bc^n_{i+1/2,j}\,\varrho^n_{i+1/2,j}(u^n_{ij} - u^n_{i+1,j}) && \text{if } K(u^2 + v^2)^n_{i+1/2,j} < (c^2)^n_{i+1/2,j} \text{ and if } u^n_{ij} > u^n_{i+1,j} \\
&= 0 \text{ otherwise} && \qquad (7)\\
q^n_{i,j+1/2} &= Bc^n_{i,j+1/2}\,\varrho^n_{i,j+1/2}(v^n_{ij} - v^n_{i,j+1}) && \text{if } K(u^2 + v^2)^n_{i,j+1/2} < (c^2)^n_{i,j+1/2} \text{ and if } v^n_{ij} > v^n_{i,j+1} \\
&= 0 \text{ otherwise.}
\end{aligned}
$$

The quantity K determines the maximum value of the Mach number at a cell interface for which the artificial viscosity term will be applied. The quantity B determines the magnitude of the viscous pressure term. It should be large enough to insure stability but small enough to avoid obscuring important details of the solution. Generally, B need not exceed a value of 0.5.

Step 2. Transport effects are now calculated. The mass which flows from cell to cell is directly proportional to the density of the donor cell (the cell from which the fluid is flowing). This has two advantages: First, it precludes the possibility that a cell can completely empty itself and develop a negative density. Second, this method, known as donor cell mass flow differencing, results in good stability properties for the far subsonic regions of the mesh.

Let $\Delta M^n_{i+1/2,j}$ be the mass flowing across the area S^z_j during the time increment δt. Similarly, let $\Delta M^n_{i,j+1/2}$ be the mass flowing across the area $S^r_{j+1/2}$. The mass flow for the right side of cell ij is then given by

$$
\begin{aligned}
\Delta M^n_{i+1/2,j} &= S^z_j\,\varrho^n_{ij}\,\tilde{u}^n_{i+1/2,j}\,\delta t && \text{if } \tilde{u}^n_{i+1/2,j} > 0\\
&= S^z_j\,\varrho^n_{i+1,j}\,\tilde{u}^n_{i+1/2,j}\,\delta t && \text{if } \tilde{u}^n_{i+1/2,j} < 0.
\end{aligned}
\qquad (8)
$$

Similarly, for the upper side of cell ij we use the relation

$$
\begin{aligned}
\Delta M^n_{i,j+1/2} &= S^r_{j+1/2}\,\varrho^n_{ij}\,\tilde{v}^n_{i,j+1/2}\,\delta t && \text{if } \tilde{v}^n_{i,j+1/2} > 0\\
&= S^r_{j+1/2}\,\varrho^n_{i,j+1}\,\tilde{v}^n_{i,j+1/2}\,\delta t && \text{if } \tilde{v}^n_{i,j+1/2} < 0.
\end{aligned}
\qquad (9)
$$

A new value for the density in cell ij can now be obtained by applying the law of conservation of mass:

$$\varrho_{ij}^{n+1} = \varrho_{ij}^{n} + \frac{1}{V_j}\left(\Delta M^{n}_{i,j-1/2} + \Delta M^{n}_{i-1/2,j} - \Delta M^{n}_{i,j+1/2} - \Delta M^{n}_{i+1/2,j}\right). \tag{10}$$

Transport of the momentum components and energy is now accomplished, assuming that the mass which crosses the cell boundaries carries the tilde velocity components and the tilde specific internal energy of the donor cell. If the four sides of cell *ij* are numbered as shown in Fig. 2, then we can define a function $T_{ij}(k)$ such that

$$\begin{aligned} T_{ij}(k) &= 1 \text{ if fluid flows into cell } ij \text{ across side } k \\ &= 0 \text{ if fluid flows out of cell } ij \text{ across side } k. \end{aligned}$$

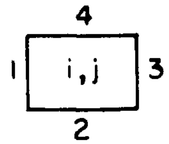

FIG. 2. Nomenclature of cell boundaries for transport calculations.

New values for the velocity components and for the energy per unit mass, *E*, which correspond to time $(n+1)\delta t$ are obtained using a general relationship of the form

$$\begin{aligned} F_{ij}^{n+1} = \frac{1}{\varrho_{ij}^{n+1} V_j} \{ & T_{ij}(1)\, \tilde{F}^{n}_{i-1,j}\, \Delta M^{n}_{i-1/2,j} + T_{ij}(2)\, \tilde{F}^{n}_{i,j-1} \Delta M^{n}_{i,j-1/2} \\ & - T_{ij}(3)\, \tilde{F}^{n}_{i+1,j}\, \Delta M^{n}_{i+1/2,j} - T_{ij}(4)\, \tilde{F}^{n}_{i,j+1}\, \Delta M^{n}_{i,j+1/2} \\ & + \tilde{F}^{n}_{ij}\, [\varrho^{n}_{ij}\, V_j + [1 - T_{ij}(1)]\, \Delta M^{n}_{i-1/2,j} + [1 - T_{ij}(2)]\, \Delta M^{n}_{i,j-1/2} \\ & - [1 - T_{ij}(3)]\, \Delta M^{n}_{i+1/2,j} - [1 - T_{ij}(4)]\, \Delta M^{n}_{i,j+1/2}]\}. \end{aligned} \tag{11}$$

Here

$$F_{ij} = \begin{Bmatrix} u_{ij} \\ v_{ij} \\ E_{ij} \end{Bmatrix}. \tag{12}$$

The specific internal energy is then found using the relation

$$I_{ij}^{n+1} = E_{ij}^{n+1} - \tfrac{1}{2}\,(u^2 + v^2)_{ij}^{n+1}. \tag{13}$$

III. Boundary Conditions

The difference equations developed in the previous section are only valid for the interior cells which are not adjacent to one of the boundaries of the computing mesh. Three types of mesh boundaries have been used: input boundaries, continuative output boundaries, and reflective boundaries. The first two of these are rather easily specified, but the last will require considerably more discussion. In all three cases the boundary criterion reduces to a determination of the values of the flow variables in fictitious cells outside the calculating mesh.

In the cells adjacent to an input boundary these values are chosen so as to represent the state of the fluid which is entering the mesh. At any given time these values are constant along the boundary but they may vary with time to represent, for example, a decaying shock wave. At a continuative output boundary the flow quantities in the fictitious boundary cells are defined in such a way that the normal space derivative of the variables vanishes at the boundary. If the output boundary coincides with cell boundaries, this merely reduces to setting the flow variables in each fictitious exterior cell equal to the value in the adjacent interior cell.

The difference equations for those cells adjacent to the bounding surface of a rigid body must be modified to insure that there is no flow of mass or energy across the boundary. This requires that the normal velocity component be zero at the body surface. In the simple case where these reflective surfaces coincide with cell boundaries, the desired boundary condition can be obtained by the use of fictitious cells. As an example, assume that the right-hand surface of cell *ij* coincides with a rigid body surface. A fictitious cell, $i + 1, j$ is used whose state at any time is completely defined by the state of cell *ij* at the corresponding time. The prescription for cell $i + 1, j$ is that the density and the specific internal energy must at all times be the same as in cell *ij*, and that the velocity must be the mirror image of that in *ij*. Thus at the end of step 1

$$\varrho^n_{i+1,j} = \varrho^n_{ij}, \qquad \tilde{I}^n_{i+1,j} = \tilde{I}^n_{ij}, \qquad \tilde{u}^n_{i+1,j} = -\tilde{u}^n_{ij}, \qquad \tilde{v}^n_{i+1,j} = \tilde{v}^n_{ij};$$

and at the end of step 2

$$\varrho^{n+1}_{i+1,j} = \varrho^{n+1}_{ij}, \qquad I^{n+1}_{i+1,j} = I^{n+1}_{ij}, \qquad u^{n+1}_{i+1,j} = -u^{n+1}_{i+1,j}, \qquad v^{n+1}_{i+1,j} = v^{n+1}_{ij}.$$

If the obstacle has a corner as shown by the shaded area in Fig. 3, the

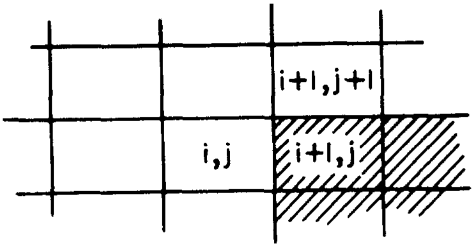

FIG. 3. Boundary cells at a corner.

fictitious cell $i + 1, j$ is assigned two sets of variables depending on whether calculations are being made for cell ij or for cell $i + 1, j + 1$.

More complicated boundary conditions are needed for a general body shape, where the body surface does not necessarily coincide with cell boundaries. A general curved boundary can be approximated as a sequence of straight lines such as is shown in Fig. 4. Each line segment then cuts across cell boundaries, which means that partial cells must be used. The partial cells thus created have a smaller volume than does a normal cell. Each partial cell is characterized by five geometrical quantities: f_{ij}, $A_{i-1/2,j}$, $A_{i+1/2,j}$, $A_{i,j-1/2}$, and $A_{i,j+1/2}$. The quantity f_{ij} is the volume fraction of the boundary cell ij which is occupied by the fluid; $A_{i-1/2,j}$ is the fraction of the area of cell ij which is open to flow between cell ij and cell $i - 1, j$, etc.

Fictitious cells are created as before to obtain the reflective boundary

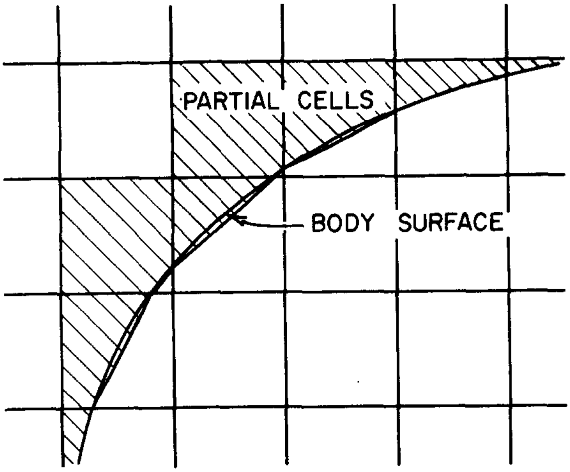

FIG. 4. Partial cells adjacent to a curved body surface.

condition. However, the difference equations must be modified to account for the smaller dimensions of the partial cells. The difference equations for calculating the tilde values of velocity and specific internal energy for partial cells are given by:

$$\tilde{u}^n_{ij} = u^n_{ij} - \frac{\delta t\, \hat{A}^z_{ij}}{\varrho^n_{ij} f_{ij}\, \delta z} \left[(P+q)^n_{i+1/2,j} - (P+q)^n_{i-1/2,j}\right] \tag{14}$$

$$\begin{aligned} \tilde{v}^n_{ij} = v^n_{ij} - \frac{\delta t\, \hat{A}^r_{ij}}{\varrho^n_{ij} f_{ij}} \Bigg[& \frac{1}{2V_j} S^r_{j+1/2} \left(P^n_{i,j+1} - P^n_{ij}\right) \\ & - S^r_{j-1/2} \left(P^n_{i,j-1} - P^n_{ij}\right) + \frac{1}{\delta r} \left(q^n_{i,j+1/2} - q^n_{i,j-1/2}\right)\Bigg] \end{aligned} \tag{15}$$

$$\begin{aligned} \tilde{I}^n_{ij} = I^n_{ij} - \frac{\delta t}{\varrho^n_{ij} f_{ij} V_j} \{ & \hat{A}^r_{ij} [P^n_{ij} (S^r_{j+1/2}\, \bar{v}^n_{i,j+1/2} - S^r_{j-1/2}\, \bar{v}^n_{i,j-1/2}) \\ & + \tfrac{1}{2} q^n_{i,j+1/2} (S^r_{j+1},\, \bar{v}^n_{i,j+1} + S^r_j\, \bar{v}^n_{ij}) \\ & - \tfrac{1}{2} q^n_{i,j-1/2} (S^r_j\, \bar{v}^n_{ij} + S^r_{j-1}\, \bar{v}^n_{i,j-1}) \\ & - \bar{v}^n_{ij}\, S^r_j (q^n_{i,j+1/2} - q^n_{i,j-1/2})] + S^z_j\, \hat{A}^z_{ij} [\bar{u}^n_{i+1/2,j} (P^n_{ij} + q^n_{i+1/2,j}) \\ & - \bar{u}^n_{i-1/2,j} (P^n_{ij} + q^n_{i-1/2,j}) - \bar{u}^n_{ij} (q^n_{i+1/2,j} - q^n_{i-1/2,j})]\}. \end{aligned} \tag{16}$$

Here,

$$\begin{aligned} \hat{A}^r_{ij} &= \text{Max}\, [A_{i,j+1/2},\ A_{i,j-1/2}] \\ \hat{A}^z_{ij} &= \text{Max}\, [A_{i+1/2,j},\ A_{i-1/2,j}]. \end{aligned} \tag{17}$$

The viscous pressure at the boundary of a partial cell is applied in a manner which is similar to that used for an interior cell except that:

a. If the cell side has part of its area open for the flow of fluid into an adajcent cell, the viscous pressure terms are calculated as if this side were entirely unobstructed.

b. If a side of cell ij is entirely closed to fluid flow, use the following prescription: If side $i + \frac{1}{2}, j$ represents a rigid boundary, then

$$\begin{aligned} q^n_{i+1/2,j} &= 2Bc^n_{ij}\, \varrho^n_{ij}\, u^n_{ij} \qquad \begin{array}{l} \text{if} \quad K(u^2+v^2)^n_{ij} < (c^2)^n_{ij} \\ \\ \text{and if} \quad u^n_{ij} > 0 \end{array} \\ &= 0 \text{ otherwise.} \end{aligned} \tag{18}$$

An analogous expression is used for $q_{i,j+1/2}$ in the case where side $i,j + \frac{1}{2}$ of cell ij is a rigid boundary.

The transport terms in step 2 are also different at a boundary cell. The mass flow terms now become

$$\begin{aligned}
\Delta M^n_{i+1/2,j} &= A_{i+1/2,j}\, S^z_j\, \varrho^n_{ij}\, \tilde{u}^n_{i+1/2,j}\, \delta t && \text{if} \quad \tilde{u}^n_{i+1/2,j} > 0 \\
&= A_{i+1/2,j}\, S^z_j\, \varrho^n_{i+1,j}\, \tilde{u}^n_{i+1/2,j}\, \delta t && \text{if} \quad \tilde{u}^n_{i+1/2,j} < 0 \\
\Delta M^n_{i,j+1/2} &= A_{i,j+1/2}\, S^r_{j+1/2}\, \varrho^n_{ij}\, \tilde{v}^n_{i,j+1/2}\, \delta t && \text{if} \quad \tilde{v}^n_{i,j+1/2} > 0 \\
&= A_{i,j+1/2}\, S^r_{j+1/2}\, \varrho^n_{i,j+1}\, \tilde{v}^n_{i,j+1/2}\, \delta t && \text{if} \quad \tilde{v}^n_{i,j+1/2} < 0.
\end{aligned} \tag{20}$$

The new value of density for the time $(n + 1)\delta t$ is given by

$$\varrho^{n+1}_i = \varrho^n_{ij} + \frac{1}{V_j f_{ij}} (\Delta M^n_{i,j-1/2} + \Delta M^n_{i-1/2,j} - \Delta M^n_{i,j+1/2} - \Delta M^n_{i+1/2,j}). \tag{21}$$

Expressions for the energy and velocity components at time $(n+1)\delta t$ are of the form

$$\begin{aligned}
F^{n+1}_{ij} = \frac{1}{V_j f_{ij} \varrho^{n+1}_{ij}} &\{T_{ij}(1)\, \tilde{F}^n_{i-1,j}\, \Delta M^n_{i-1/2,j} + T_{ij}(2)\, \tilde{F}^n_{i,j-1}\, \Delta M^n_{i,j-1/2} \\
&- T_{ij}(3)\, \tilde{F}^n_{i+1,j}\, \Delta M^n_{i+1/2,j} - T_{ij}(4)\, \tilde{F}^n_{i,j+1}\, \Delta M^n_{i,j+1/2} \\
&+ \tilde{F}^n_{ij}[\varrho^n_{ij} f_{ij}\, V_j + [1 - T_{ij}(1)]\Delta M^n_{i-1/2,j} + [1 - T_{ij}(2)]\Delta M^n_{i,j-1/2} \\
&- [1 - T_{ij}(3)]\, \Delta M^n_{i+1/2,j} - [1 - T_{ij}(4)]\, \Delta M^n_{i,j+1/2}]\}.
\end{aligned} \tag{22}$$

As before,

$$F_{ij} = \begin{Bmatrix} u_{ij} \\ v_{ij} \\ E_{ij} \end{Bmatrix}. \tag{23}$$

The use of partial cells can cause difficulty in cases where they are much smaller than full sized cells. Since the maximum value of δt is limited for stability and accuracy reasons by the minimum cell dimension, these small partial cells could lead to prohibitively long calculation times. Such extremely small partial cells should therefore be avoided whenever possible. If these small cells should prove to be essential, then the time limitations may be overcome by using more computing cycles per unit time for the partial cells than for the rest of the mesh.

IV. Stability and Accuracy

The use of finite difference equations introduces truncation errors which are determined by the size of δx and δt. Furthermore, the artificial viscosity term which is added for computational stability also introduces errors into the solutions. If the difference equations are stable, then errors related to the finite size of δt are usually small, since the relative change of the cellwise variables which occurs in a time step is usually small. On the other hand, the truncation errors related to the finite size of the mesh cells are more likely to be important, since limitations of machine storage and running time make it necessary to use a fairly coarse computing mesh for two-dimensional problems.

The dominant error terms that are introduced by the numerical approximations can be obtained by performing a Taylor expansion of the finite difference equations, neglecting all terms which are of order δt or δx^2. The form of these error terms is shown below for the case where the solution is a function of one space variable and time:

Artificial viscosity terms

Truncation error terms

$$\frac{D\varrho}{Dt} + \varrho \frac{\partial u}{\partial x} = \quad \cdots \quad + \frac{\partial}{\partial x}\left(\varepsilon \frac{\partial \varrho}{\partial x}\right) \tag{24}$$

$$\varrho \frac{Du}{Dt} + \frac{\partial P}{\partial x} = -\frac{\partial q}{\partial x} + \frac{\partial}{\partial x}\left(\varrho\varepsilon \frac{\partial u}{\partial x}\right) + \varepsilon \frac{\partial \varrho}{\partial x}\frac{\partial u}{\partial x} \tag{25}$$

$$\varrho \frac{DI}{Dt} + P \frac{\partial u}{\partial x} = -q \frac{\partial u}{\partial x} + \frac{\partial}{\partial x}\left(\varrho\varepsilon \frac{\partial I}{\partial x}\right) + \varrho\varepsilon \left(\frac{\partial u}{\partial x}\right)^2 + \varepsilon \frac{\partial \varrho}{\partial x}\frac{\partial I}{\partial x}. \tag{26}$$

Here,

$$\varepsilon = \tfrac{1}{2}\, |u|\, \delta x. \tag{27}$$

The correct terms in the equations of motion of the fluid are given on the left side of Eqs. (24), (25), and (26), and the dominant error terms appear on the right-hand side. There are two types of error terms: Artificial viscosity terms which contain q and $\partial q/\partial x$, and truncation terms, which contain ε and $\partial \varepsilon/\partial x$. The effect of the error terms is to cause an artificial diffusion of mass, momentum, and energy to occur in regions where there are large variations. Actually,s ome of the terms are similar to those which would be present if bulk viscosity and heat conduction effects were included. Consider, for example, the term $\partial/\partial x(\varrho\varepsilon\partial u/\partial x)$

which appears in the momentum equation. Here the quantity ε plays the role of the bulk viscosity. The terms $\partial/\partial x(\varrho\varepsilon\partial I/\partial x)$ and $\varrho\varepsilon(\partial u/\partial x)^2$ that appear in the energy equation are analogous to the heat conduction and viscous dissipation terms which occur in the flow of real fluids. The right-most terms which appear in the three equations are artificial mass diffusion terms.

These errors cause shocks to smear much in the same manner as would ordinary viscosity and heat conduction effects. However, there are several important differences. First, since ε is proportional to δx, the shock thickness will be determined by δx in contrast to the case for real gases, where it is determined by the microscopic mean free path for diffusion processes. Also, the effective "viscosity" is proportional to $|\mathbf{u}|$, the magnitude of the local velocity of the fluid relative to the computing mesh. This is nonphysical since a term of this type destroys the Galilean invariance of the solution.

The effects of the two types of differencing errors can be seen in the plots shown in Fig. 5. Here the IBM 7030 ("Stretch") computer has been used to obtain the solution for axi-symmetric flow past a flat-faced cylindrical body at a Mach number of 3.15. The Stromberg-Carlson SC 4020 plotter has been used to plot the pressure contours (isobars), the density contours (isopycnics), and the specific internal energy (S.I.E.) contours for the numerical solution. The upper row of plots shows the solution for a case where the artificial viscosity term is zero. The smearing of the bow shock is a result of the diffusion effects caused by the truncation errors. The lower row of plots depicts a solution which is similar in all respects except that artificial viscostiy has been included. (Here, B has a value of 0.5.) It can be seen that the additional diffusion effects caused by the artificial viscosity result in an additional smearing of the detached shock. Also evident here is an entropy increase in the region of the flat body surface which is characteristic of numerical solutions involving the use of artificial viscosity. This is demonstrated by an increase in the specific internal energy at the body surface which is offset by a decrease in the fluid density, leaving the surface pressure essentially unchanged. This effect has been observed in a number of problems involving the interaction of a fluid with a rigid boundary.

The effects of the truncation errors on Galilean invariance can be seen by considering a particular example. Consider two problems which are identical except that the velodities in the second differ everywhere from those in the first by a constant value, say $\mathbf{U}_0$. The numerical solu-

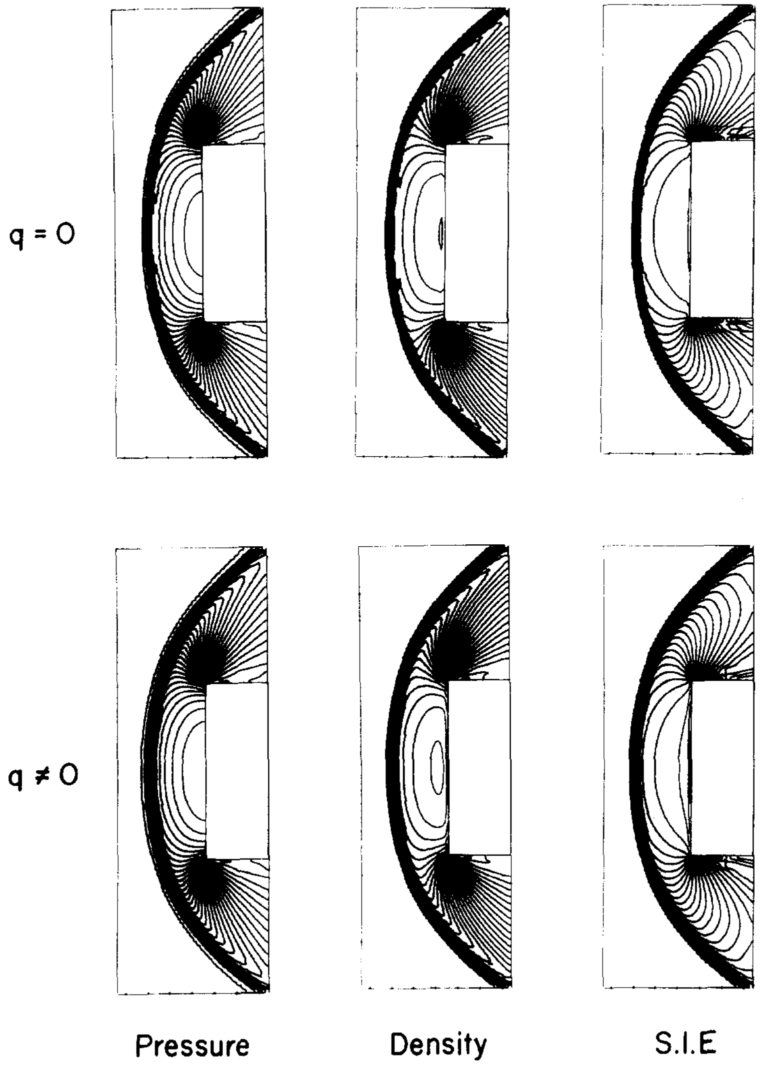

FIG. 5. Computer-drawn plots which depict the numerical solution for steady flow past a blunt body at a Mach number of 3.15.

tions which would be obtained for these problems will show another important difference. Since the cellwise values of ε are different for the two calculations, the diffusion effects caused by the truncation errors will also be different. If U_0 increases the local magnitude of the fluid velocity, for instance, than it will increase ε and hence increase the amount of smearing caused by the truncation errors. This effect is illustrated in Fig. 6, which compares the calculated profiles of two shocks characterized by a shock Mach number of 2.0. Here the fluid has a value of γ equal to 1.4. Pressure and velocity are plotted as a function of distance, where the distance is measured in units of δx, the cell width. In the first case, represented by the unbroken line, the shock is propagating into a fluid at rest. In the second case, the fluid velocity ahead of the shock is equal to one half the shock velocity used in the first solution. Greater smearing is evident at the shock front for the second solution. This is caused by the additional diffusion effects which result from the increase in velocity relative to the computing mesh.

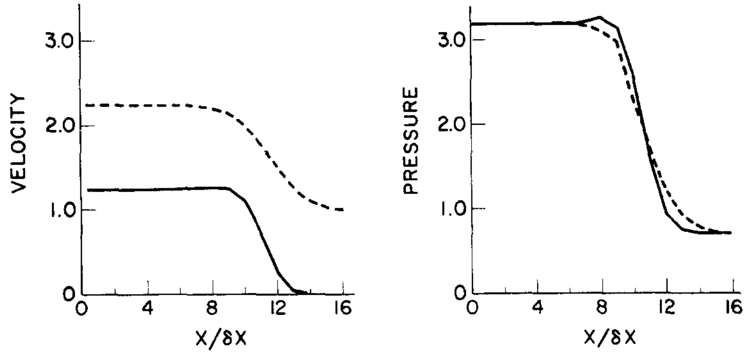

FIG. 6. Calculated velocity and pressure profiles for two shocks propagating with different velocities relative to the computing mesh. In each case the shock Mach number is equal to 2.0.

For many problems the detailed structure of discontinuities such as shocks and contact surfaces are not important. For these cases, the effect of the truncation errors can be reduced to a satisfactory level by choosing δx to be small compared with the characteristic lengths associated with the important features of the solution.

The truncation error terms which appear on the right-hand side of Eqs. (24), (25), and (26) can be eliminated, leaving only terms of order δx^2, by altering the methods used in step 2 for calculating transport effects. The artificial mass diffusion terms, which are the rightmost terms, can be eliminated by using the average density at a cell boundary to calculate the mass flow that occurs across the cell boundary during the time step δt. Similarly, the "viscosity" and "heat conduction" error terms can be eliminated by using the boundary cell averages of the velocity and specific internal energy to compute the transport of momentum and energy across the cell boundaries. Thus the use of boundary cell averages appears at first glance to be of higher order accuracy than the donor cell method. However, it leads to a set of difference equations which have undesirable stability properties. In addition, the use of boundary cell averages can lead to negative cell densities.

The time step is usually chosen such that

$$\frac{|\mathbf{u}|\,\delta t}{\delta x} < 0.4 \tag{28}$$

to insure accurate solutions. In addition to this requirement other conditions must be met to insure computational stability. A one-dimensional linear stability analysis for the stagnation region indicates that the following inequalities must hold in order to insure a stable solution:

$$\frac{c\,\delta t}{\delta x} < \lambda_{\min}\,, \tag{29}$$

where

$$\lambda_{\min} = \mathrm{Min}\,[1 < B,\ -\gamma B + (\gamma^2 B^2 + 4\gamma)^{1/2}, \gamma B/(\gamma - 1)]. \tag{30}$$

(See Harlow [5] and Richtmyer [6] for a discussion of the linear stability analysis for finite difference equations.) Several of the stability modes which occur have been observed in one-dimensional test problems. The above condition indicates that the difference scheme is unconditionally unstable if B is zero, i.e., if the artificial viscosity is zero. We find, however, that in certain types of two-dimensional problems a stable solution can be obtained in the absence of artificial viscosity. The blunt body problem shown earlier demonstrates this.

V. APPLICATIONS OF THE FLIC METHOD

Butler [7] recently used the FLIC method to compute the interaction of plane shocks with rectangular obstacles and axi-symmetric blunt bodies. He was able to obtain very good agreement with photographic data obtained by Bleakney [8] for the diffraction of a weak shock by a rectangular body. Three recent investigations are described below to illustrate the applicability of the method. In each case the solution was obtained using an IBM 7030 ("Stretch") computer. The plots shown were made by incorporating a special plot routine into the program and processing the output through the Stromberg-Carlson SC-4020 Microfilm Recorder.

Diffraction of a Shock by a z-Shaped Tunnel. Reichenbach [9] and Daly *et al.* [10] recently studied the effect of a z-shaped tunnel in reducing the strength of the reflected shock which reaches a bomb shelter door, located at the end of the tunnel. Reichenbach's shock tube experiments, with which we compare our numerical results, made use of the scale model of the tunnel shown in Fig. 7. In order to determine the reduction in the strength of the shock resulting from its passage around the corners of the tunnel, he made continuous pressure measurements at points 1 and 2 as shown in Fig. 7. The width of the experimental tunnel was 2 cm, and the lengths of the first and second legs were respectively 8 and 8.8 cm. A deposit plate was located in the mouth of the channel in order to obtain a uniform input pressure.

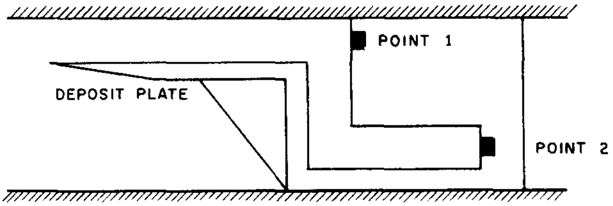

FIG. 7. Scale model of the shelter access tunnel used by Reichenbach in his shock tube experiments.

A numerical solution has been obtained which simulates this experiment using a boundary configuration which is identical with that of the experiment. An input channel, of approximately the same length as that formed by the deposit plate in the experiment, is also included in the calculational mesh. The problem begins with shocked material filling the input channel and with air at standard atmospheric conditions in both legs of the tunnel. The input conditions for the mesh do not change with time. Pressure data are obtained from the calculations at the same two points as in the shock tube experiments.

The calculation cells are square, 2 mm on a side. The 2-cm channel width is therefore divided into ten cells and there are 1270 calculation [illegible]

[illegible] over-pressures at point 1 for a case in which the incoming shock had an overpressure of 1.29 atmospheres. Figure 9 shows the corresponding overpressure at point 2. The calculated overpressures are indicated by

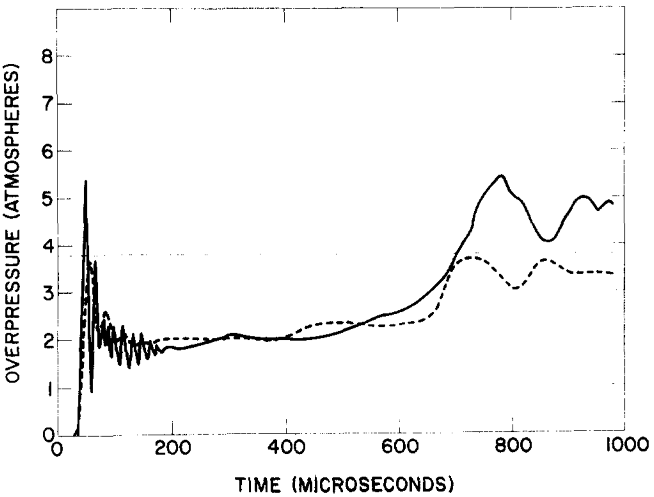

FIG. 8. Comparison of experimental and calculated tunnel pressure histories at point 1.

heavy dashed lines, and the solid lines represent experimental results. (The original experimental data showed only maximum and minimum lines in the region of large fluctuation following the shock reflection at 1. The curves shown, which fit these extremal lines, were substituted for the purpose of clarity.) The light, horizontal dashed line indicates the

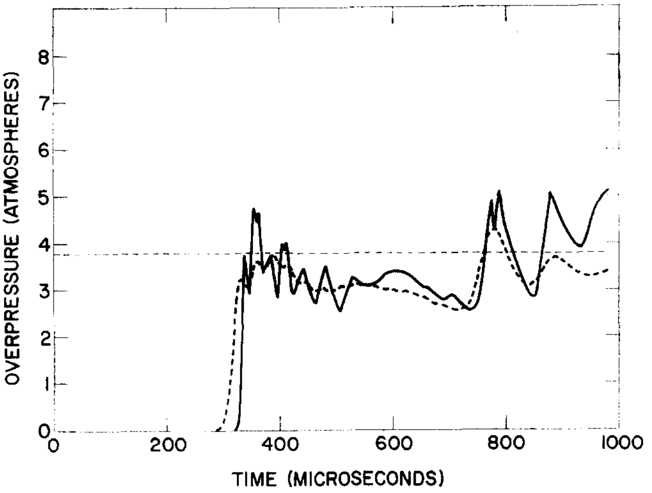

FIG. 9. Comparison of experimental and calculated tunnel pressure histories at point 2.

overpressure which would be observed if the incoming shock reflected normally from a semi-infinite wall. It is included here as a reference magnitude with which the other curves may be compared.

The time $t = 0$ in these figures corresponds to the time at which the calculation was initiated. Initial time for the experimental curve was chosen in such a way that the time of the first significant overpressure measurement at point 1 was in agreement between calculation and experiment. No adjustments were made to the timing of any subsequent measurements.

The agreement between calculated and experimental overpressure curves is good in regard to magnitude, timing and curve shape until late times.

At early times one can see that the magnitudes of the calculated pressure peaks produced by the incoming shock are slightly less than the overpressures which would be produced by a one-dimensional reflection. Because of two-dimensional effects, this is what one would expect. The first peaks on the experimental curves overshoot this maximum value. These must be spurious, however, since the initial pressures should not exceed the value predicted by the one-dimensional normal shock reflection theory. Subsequent to this overshoot, the calculated and experimental values decay in amplitude at the same rate.

After these initial fluctuations, the two curves remain close to the same level and are in generally good agreement until the reflected shock returns from the end of the channel. Both curves give evidence of the arrival of this strong shock, but a comparison shows inconsistencies in regard to both curve shape and magnitude at late times. This discrepancy occurs because at late times the simple input conditions used for the calculations no longer represent the upstream conditions of the shock tube. The initial shock, which was deflected from the tunnel opening by the deposit plate (see Fig. 7) has reflected from the tunnel model and completely encompasses the deposit plate. As a result, a much stronger shock is now present in the input channel of the test model. This causes a boost in the overpressure at point 1 and completely alters the flow field in the channel. Further comparison of calculation and experiment is therefore impossible.

The initial pressure pulse recorded at point 2 (Fig. 9) has two outstanding characteristics: the initial value of the overpressure is slightly higher than the first pulse at point 1, and the duration of the high-pressure phase is much longer than it is at point 1. Since the tunnel terminates at point 2, the long duration of the pulse is to be expected, but the fact that the shock strength does not decay as a result of the bends in the channel is at first glance rather surprising, since it indicates that the use of a *z*-shaped tunnel is a hinderance rather than a help in reducing the reflected shock pressure. The reason for this can be seen by looking at the various shocks which travel down the tunnel.

Figure 10 shows a series of six computer-produced isopycnic contour plots. The times in these plots correspond to the times of Figs. 8 and 9. The closeness of the contours gives a measure of the density gradient and thereby enables us to locate shock fronts.

The calculation begins with a plane shock at the end of the input channel. In the second plot this shock expands into the first leg of the tunnel. A part of it reflects at point 1 while the remainder proceeds downstream. (The initial shock and the reflected shock are labeled S_I and S_R, respectively, in the diagrams.) At $t = 100$, this weakened initial shock is near the second corner and the downstream part of the reflected shock is overtaking it. The part of the reflected shock which is moving upstream proceeds more slowly since it moves against the flow.

In the fourth plot the combined initial and reflected shocks have expanded about the second corner and repeat the phenomenon which was observed at the first corner. The vortices which develop in the expanding flow at the corners are evident in this and the next two plots. Also evident in the final two plots is the reflected shock which is moving away from the second tunnel corner. This reflected shock overtakes and strengthens the leading shock. The resulting shock reaches the end of the tunnel before it can be weakened by a reflected rarefaction. As a result we observe a higher initial overpressure at point 2 than we do at point 1.

The Shock-on-Shock Problem. When a blunt body in steady supersonic motion meets a plane shock wave, the interaction of the detached bow shock with the plane shock causes the formation of two shocks which move toward the body. When the faster moving shock reaches the body, high surface pressures are produced. Eventually these high surface pressures are relieved as rarefactions move across the body surface, permitting the establishment of a new steady flow regime. Recently the FLIC method was used to calculate the flow which occurs in the region surrounding the nose of a supersonic blunt body during shock immersion in order to determine the amplitude and duration of the transient pressure field which occurs at early times. A typical solution is described below.

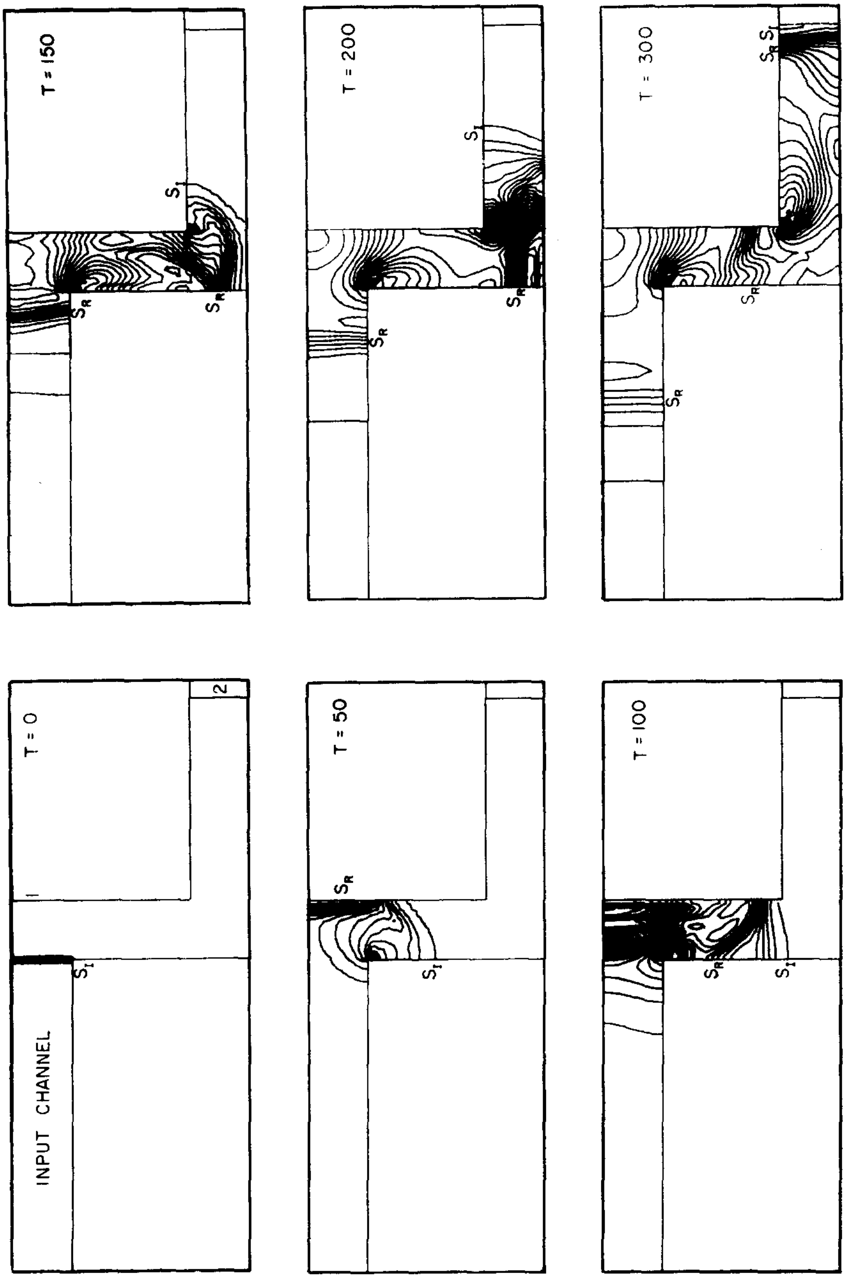

FIG. 10. Isopycnic contours depicting the motion of a weak shock as it travels through the shelter access tunnel.

Consider the immersion of a supersonic flat faced cylinder in a plane shock as shown in Fig. 11. The initial steady supersonic motion at a Mach number M_1 has caused the formation of a detached shock as shown in the left-hand picture. When the detached bow shock meets the plane shock, two shocks and a contact surface are formed as shown in the center picture. They then move toward the flat surface of the body. Eventually the faster moving shock reaches the body surface and is reflected, as in shown in the right-hand picture. At this time there is a sharp rise in the surface pressure. The high surface pressure will last until rarefactions relieve them.

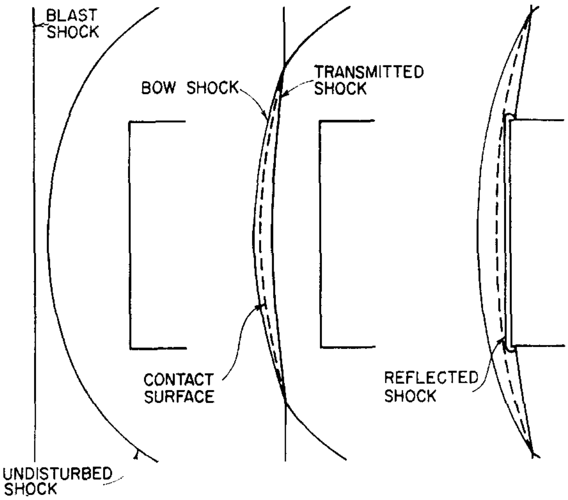

FIG. 11. Description of the shocks and contact surface which form around the nose region of a blunt supersonic body during the early stages of shock immersion.

As soon as the first shock reflection occurs, a rarefaction will begin to move inward radially toward the stagnation point, located at the intersection of the symmetry axis with the body surface. The reflected shock soon interacts with the contact surface, sending either a shock or a rarefaction back to the body surface, as well as a transmitted shock which moves away from the body toward the bow shock. Eventually this transmitted shock reaches the bow shock and sends another rarefaction back that further relieves the surface pressure. After the arrival of the last rarefaction, a steady flow region gradually forms.

For this calculation two separate solutions must be obtained. The steady flow solution at a Mach number of M_1 is first computed. This is accomplished by beginning with an arbitrary mesh configuration and by specifying a steady flow at Mach number M_1 as the input boundary condition at the upstream side of the mesh. The flow field then passes through a transient phase, eventually reaching the desired steady solution. In certain cases the calculation is begun using identical values for the fluid field variables in each mesh cell. Although this type of initial condition has the virtue of simplicity, it probably adds somewhat to the computer time that is necessary to obtain the steady flow solution. In some cases it is possible to use a previous solution as a starting condition by suitably changing the upstream boundary conditions, and then letting the flow field relax to the new solution. After the detached shock has formed and the field variables no longer change with time, the boundary conditions in the upstream input cells are changed discontinuously to the desired solution of the Rankine-Hugoniot equations describing the new plane shock wave, characterized by the shock Mach number, M_s. A plane shock then forms naturally at the upstream edge of the mesh and moves across the mesh towards the detached bow shock. The transient phase of the so-called "shock-on-shock" process begins when the two shocks meet.

Figure 12 shows the isobar contour plots for a solution in which $M_1 = M_2 = 3.15$. Here δr and δz are equal to $0.05R$ and $0.025R$, respectively, where R is the body radius. The upstream flow conditions are chosen such that the input density and sound speed are unity. We use a polytropic equation of state for air with γ equal to 1.4. This is a good approximation for relatively weak shocks, as will be shown below. The first picture in the upper left-hand corner of Fig. 12 shows the undisturbed bow shock. The second picture depicts the flow field shortly after shock intersection. The two shocks which form when the bow shock and the plane shock interact can be seen here, as can the undisturbed plane shock at the upper and lower portions of the mesh. In the third picture the faster moving shock has reflected at the body surface and is moving away from the body toward the bow shock. In the fourth and fifth pictures, a rarefaction is visible that is moving inward radially toward the stagnation point. The sixth picture depicts the flow field at late times when a new steady flow solution has formed. Note that the shape of the bow shock is different at late times than it was before the passage of the plane shock. This is because the upstream Mach number has increased from a value of 3.15 to a value of 3.26.

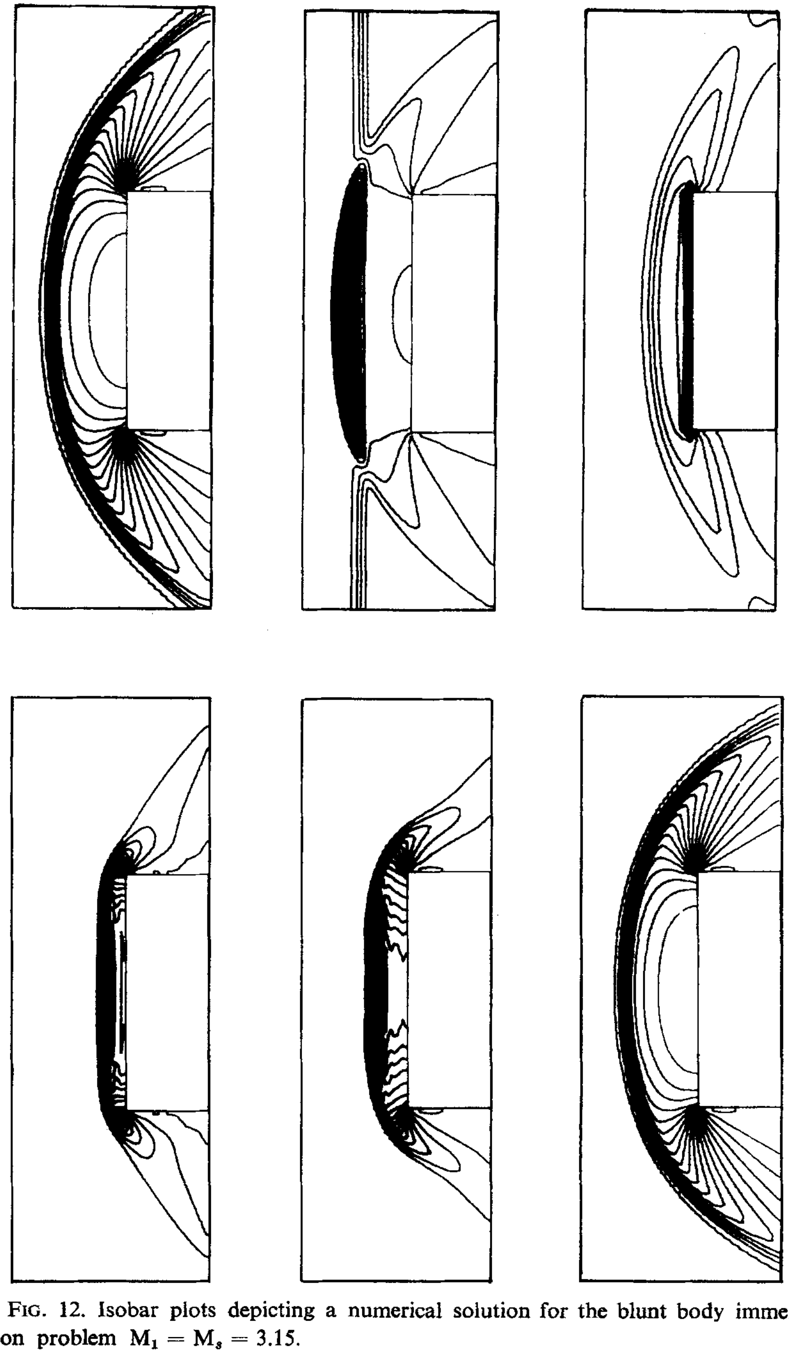

FIG. 12. Isobar plots depicting a numerical solution for the blunt body immersion problem $M_1 = M_s = 3.15$.

The results of this calculation compare favorably with some previously unpublished experimental data obtained recently by Merritt and Aronson [11], who have obtained shock-on-shock data for various body shapes by mounting a shock tube in a wind tunnel settling chamber upstream from the model [12]. Figure 13 shows the stagnation pressure ratio plotted as a function of time. The time unit has been chosen so that the plane shock, moving at a velocity U_s relative to the body, moves 1 body radius per time unit. The dashed line represents the computed results and the solid line represents the scaled experimental pressure record obtained by Merritt and Aronson. They agree very well for times less than 3.0. The experimental pressure drops at late time because of the finite duration of the shock tube experiment.

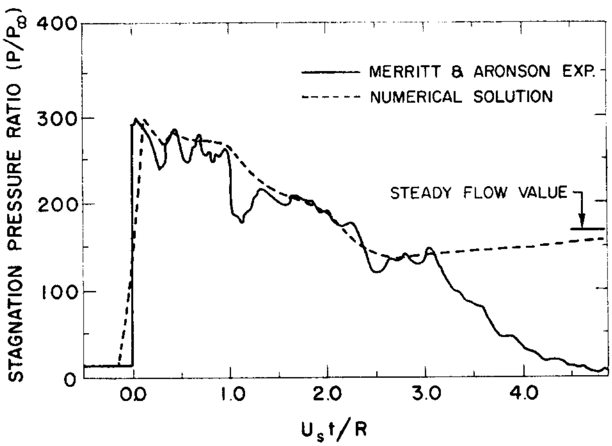

FIG. 13. Experimental and computed stagnation pressure history. $M_1 = M_s = 3.15$.

The first drop in the stagnation pressure at a time of 1.0 is caused by the arrival of the axially moving rarefaction which was transmitted back to the body when the reflected shock reached the bow shock. The second pressure drop at a time of 2.4 is caused by the arrival of the radially moving rarefaction that formed at the outer edge of the body at the time of the first shock reflection. Note that the reflection of this rarefaction at the symmetry axis causes a pressure undershoot. After the arrival of the second rarefaction, the stagnation pressure gradually rises to its final steady flow value. The late time stagnation pressure, calculated from Bernouli's law and the Rankine-Hugoniot equations for the bow shock, is shown on the plot. The calculated value of the stagnation pressure has not quite reached this value at the time the calculation is stopped.

Figure 14 shows the positions of the various shocks at the time of the first shock reflection. The dark lines are taken from photographic data

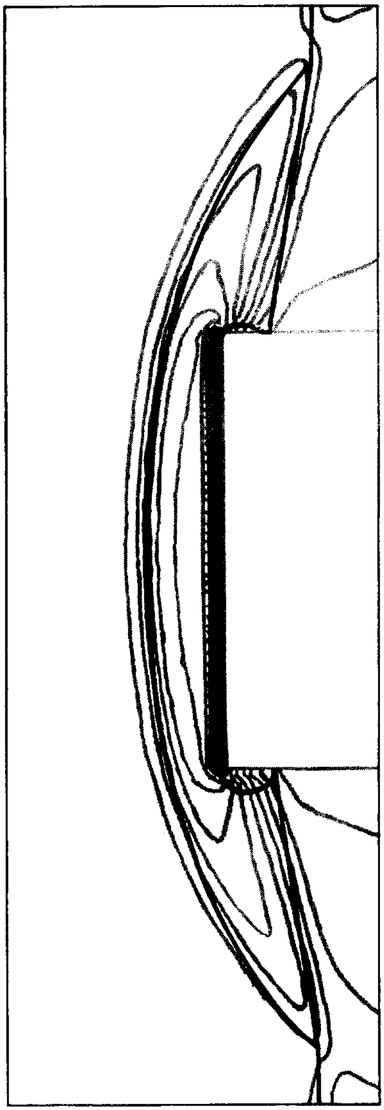

FIG. 14. Measured and calculated shock positions at the time of first shock reflection. $M_1 = M_s = 3.15$.

obtained by Merritt and Aronson, and the light grey lines are isopycnic lines plotted from the corresponding numerical solution.

The computed pressure ratios for the flat body surface are plotted as a function of the scaled radius for several times in Fig. 15. Note that the shock first arrives at the outer radius of the body, as shown by the high pressures at large radii in the zero time plot. The plots at times of 0.554 and 1.11 show the rapid relief of the pressure at the outer body radii, and the motion of the rarefaction as it travels inward toward the stagnation point. The pressure plot at a time of 2.49 shows the further decrease in the surface pressure in the neighborhood of the stagnation point caused by reflection of the rarefaction at the symmetry

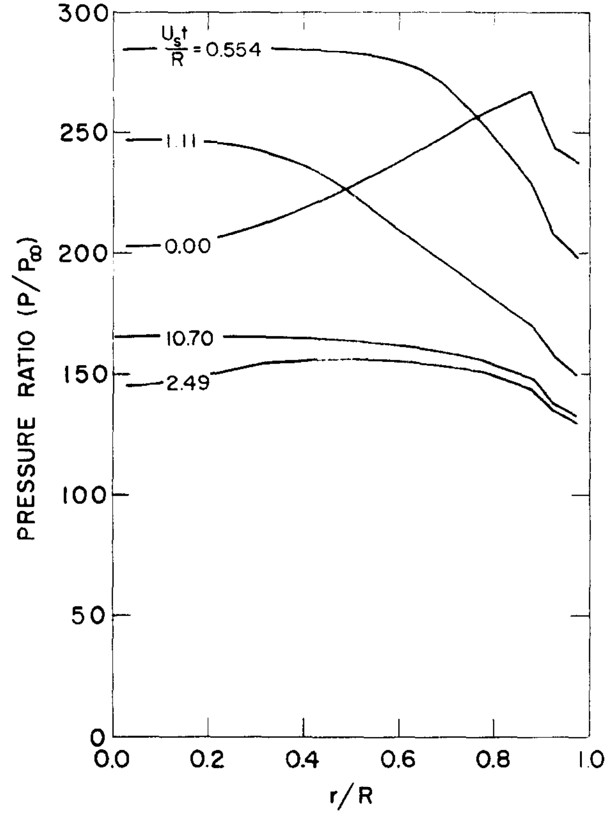

FIG. 15. Computed surface pressure ratio vs. scaled radius for several times after shock immersion. $M_1 = M_s = 3.15$.

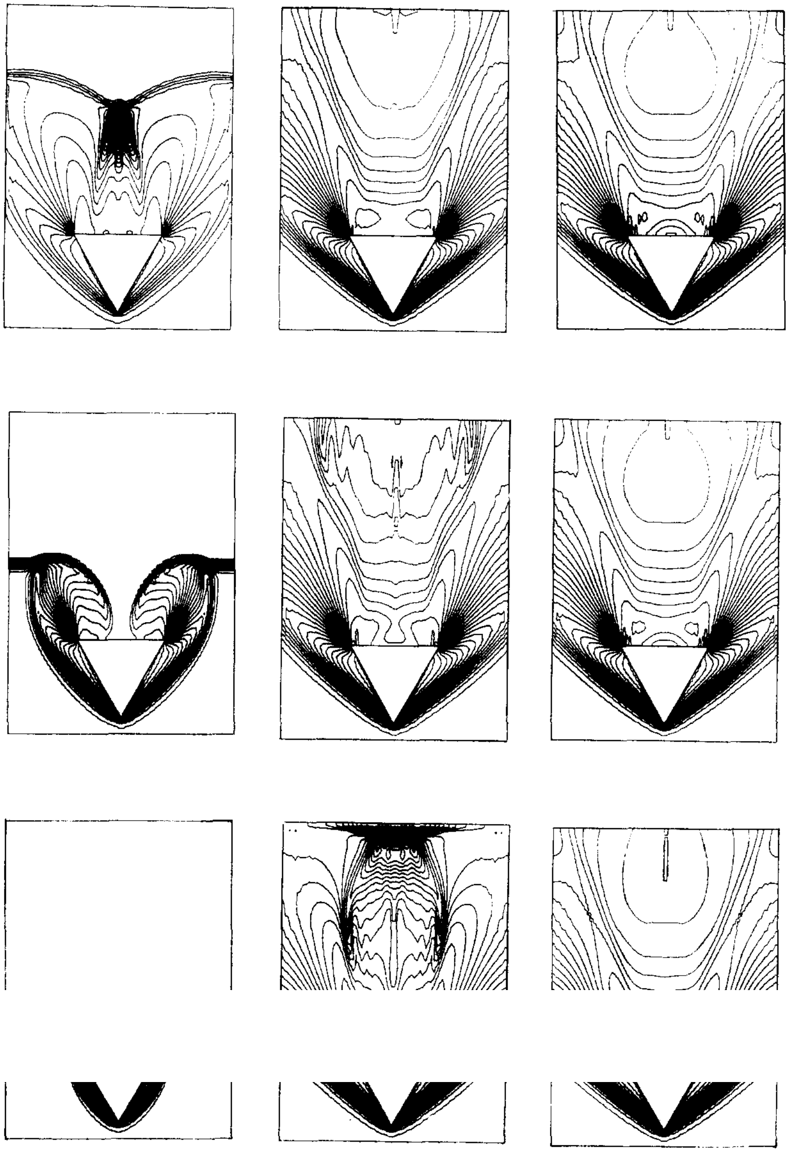

F sobar plots depicting the passage of an infinite strength shock over a 30° half angle cone.

axis. The late time plot depicts the surface pressure distribution for steady flow at the new value of the upstream Mach number, which is 3.26 after the passage of the plane shock.

Diffraction of a Plane Shock by a Cone. In certain cases, partial cells can be used in obtaining satisfactory solutions. This is illustrated in the final example, which simulates the passage of an infinite strength plane shock over a 30° half angle cone. Here the fluid ahead of the shock is cold and at rest. As in the earlier problems, γ is equal to 1.4. In order to eliminate partial cells with small fractional volumes, the mesh has been chosen such that the conical surface coincides with diagonals drawn through the corners of the mesh cells. This means that each of the partial cells adjacent to the conical surface has a fractional volume of approximately one-half. To accomplish the desired cone shape, the aspect ratio of the mesh cells, $\delta r/\delta z$, was set equal to the tangent of the cone half angle. For the example shown below $\delta r = R/16$, where R is the cone base radius.

Figure 16 shows a series of nine computer-drawn isobar plots, illustrating the development in time of the numerical solution. The time interval between plots is L/U_s, where L is the body length and U_s is the velocity of the plane shock relative to the body. (The plane shock moves one body length during the time interval between each consecutive plot.) The plane shock has nearly reached the cone base in the first plot in the upper left-hand corner. Also evident is the shock caused by reflection at the cone surface. As the plane shock moves aft past the cone base, the reflected shock moves outward radially to form a standing bow shock which is attached at the apex of the cone. This radial motion is evident in the second plot. By this time the shock has also diffracted around the base of the cone and is converging on the symmetry axis, as can be seen in the second plot. When the diffracted shock converges on the symmetry axis, a high pressure region forms near the cone base, causing another shock to move outward from the symmetry axis. This can be seen in the third plot. The bow shock shown in the fourth plot remains essentially unchanged at later times, as do the flow variables in the neighborhood of the conical surface. The flow field in the base region of the cone continues to change slowly for a much longer time, as can be seen in the following five plots. Figure 17 depicts contour plots at a very late time when steady flow has been established.

It can be seen that the conical bow shock is poorly defined in the region near the apex of the cone. This is to be expected, since here the

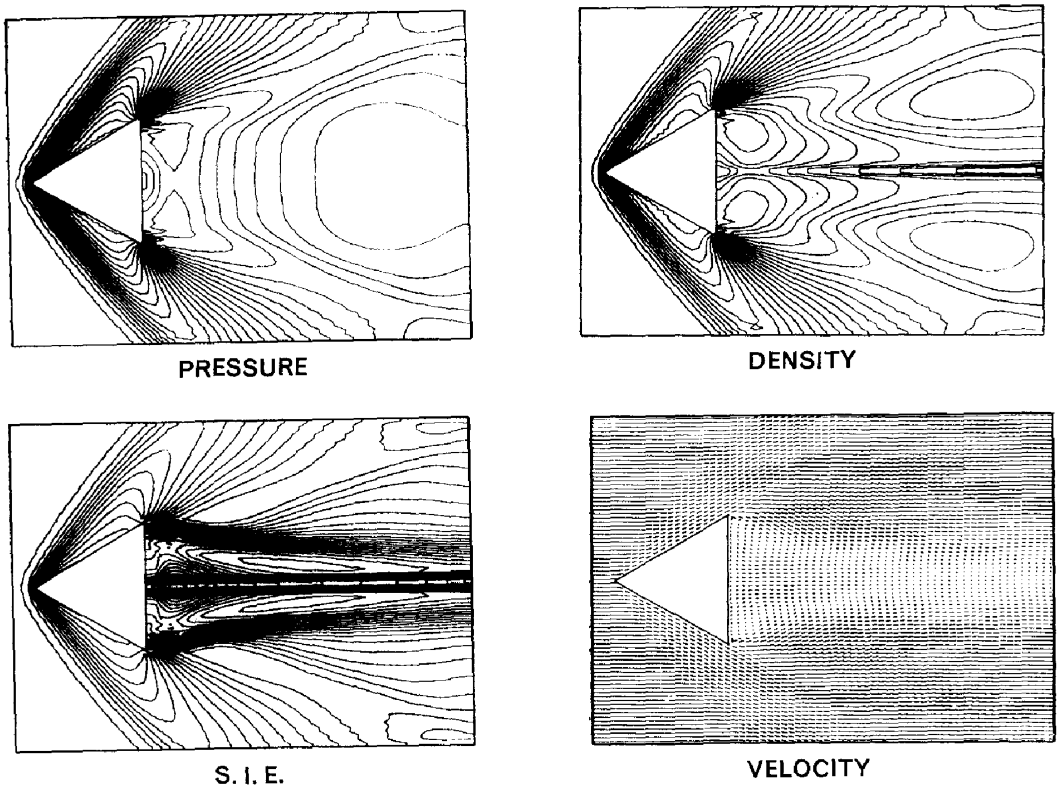

FIG. 17. Late time contour plots which depict the steady flow field in the vicinity of the cone.

region between the cone surface and the bow shock is smaller than the dimensions of a mesh cell. However, experience with several conical flow problems has shown that the solutions obtained for the regions aft of the apex, where good resolution is possible, are accurate. The late time surface pressures on the conical surface in the region approximately one-half body length aft of the apex are within 2% of the value obtained by Kopal for steady flow past an infinite cone [13].

VI. CONCLUDING REMARKS

The outstanding characteristic of the FLIC method is that it can provide accurate solutions for complicated fluid flow problems with a relatively modest investment in computer time. It is most suitable for one material problems involving large fluid distortions. Surprisingly good results have been obtained in some applications using a relatively coarse mesh. This was demonstrated by the shelter tunnel problem described above.

ACKNOWLEDGMENTS

The authors wish to express their sincere appreciation for the encouragement and invaluable guidance extended by Dr. Francis H. Harlow during the preparation of this paper. We are also indebted to Dr. Reichenbach of the Ernst Mach Institute and Drs. Merritt and Aronson of the U.S. Naval Ordnance Laboratory for their kindness in permitting the inclusion of previously unpublished experimental data. This work was performed under the auspices of the U.S. Atomic Energy Commission.

REFERENCES

1. F. H. HARLOW, *in* "Experimental Arithmetic, High Speed Computing and Mathematics" (Proceedings of Symposia in Applied Mathematics) (N. C. Metropolis, A. H. Taub, John Todd, and C. B. Tompkins, eds.); Vol. 15, p. 269. American Mathematical Society, Providence, Rhode Island (1963).
2. F. H. HARLOW, *in* "Methods of Computational Physics" (B. Alder, S. Fernbach, and M. Rotenberg, eds.), Vol. 3, p. 319. Academic Press, New York (1964).
3. M. RICH, "A Method for Eulerian Fluid Dynamics," Report No. LAMS-2826. Los Alamos Scientific Laboratory (1963).
4. B. J. DALY, "The Bounding of Instabilities of the PIC Difference Equations," Report No. LA-2414, Appendix I. Los Alamos Scientific Laboratory (1962).

5. F. H. Harlow, "Stability of Difference Equations, Selected Topics," Report No. LAMS-2452. Los Alamos Scientific Laboratory (1960).

6. R. D. Richtmyer, *in* "Difference Methods for Initial-Value Problems," Wiley (Interscience), New York (1957).

7. T. D. Butler, "Numerical Calculations of the Transient Loading of Blunt Obstacles by Shocks in Air." Accepted for publication in the AIAA Journal.

8. W. Bleakney, "The Diffraction of Shock Waves Around Obstacles and the Transient Loading of Structures," Technical Report No. II-3. Princeton Univ. Department of Physics, Princeton, New Jersey (1950).

9. H. Reichenbach, Ernst-Mach Institute, Frieburg, Germany; private communication (1965).

10. B. J. Daly, F. H. Harlow, and J. E. Welch, "Numerical Fluid Dynamics Using the Particle-And-Force Method," Report No. LA-3144, p. 62. Los Alamos Scientific Laboratory (1965).

11. D. L. Merritt and P. M. Aronson, "Study of Blast-Bow Wave Interactions in a Wind Tunnel," AIAA Paper No. 65-5, presented at the AIAA Second Aerospace Sciences Meeting, New York, N. Y., January 25–27, 1965.

12. D. L. Merritt and P. M. Aronson, U.S. Naval Ordnance Laboratory, Silver Spring, Maryland; private communication (1965).

13. Z. Kopal, "Tables of Supersonic Flow Around Cones," Technical Report No. 1. Massachusetts Institute of Technology Dept. of Electrical Engineering, Cambridge, Massachusetts (1947).